

# Tailored Spiral In-Out Spectral-Spatial Water Suppression Pulses for Magnetic Resonance Spectroscopic Imaging

Jun Ma<sup>1,3</sup>, Carrie Wismans<sup>2</sup>, Zhipeng Cao<sup>1</sup>, Dennis W.J. Klomp<sup>2</sup>, Jannie P. Wijnen<sup>2</sup>  
and William A. Grissom<sup>\*1,3</sup>

August 6, 2020

<sup>1</sup>Vanderbilt University Institute of Imaging Science, Nashville, TN, United States

<sup>2</sup>Department of Radiology, University Medical Centre Utrecht, Utrecht, the Netherlands

<sup>3</sup>Department of Biomedical Engineering, Vanderbilt University, Nashville, TN, United States

---

Word Count: Approximately 3550

\*Corresponding author:

Will Grissom

Department of Biomedical Engineering

Vanderbilt University

5824 Stevenson Center

Nashville, TN 37235 USA

E-mail: will.grissom@vanderbilt.edu

Twitter: @wgrissom

Submitted to Magnetic Resonance in Medicine for consideration as a Full Paper.

Acknowledgment: This work was supported by NIH R01 EB016695.

## **Abstract**

**Purpose:** something

**Methods:** something

**Results:** something

**Conclusion:** something

**Key words:** Spectroscopy; RF pulses; Ultra-high field MRI; RF pulse design; Selective excitation; Optimization.

## Introduction

Multidimensional RF pulses have been widely used in many applications such as reduced field-of-view imaging [1], transmit field inhomogeneity correction [2], and susceptibility artifacts correction [3]. Parallel transmission (pTx) [4, 5] further strengthens the multidimensional pulses by providing extra spatial encoding power, shortening pulse duration, and reducing specific absorption rate (SAR). However, current multidimensional pTx pulse design methods are based on a spatial domain formulation [6, 7] that has prohibitive memory and computational requirements when the number of coils and the number of dimensions both become larger in current designs. Particularly, current spatial domain design methods map any given RF pulse  $\mathbf{b}$  to its spatial excitation pattern  $\mathbf{d}$  with a large system matrix  $\mathbf{A}$ , as:

$$\mathbf{d} = \mathbf{Ab}$$

The size of  $\mathbf{A}$  is  $N_s$  by  $N_c N_t$ , where  $N_s$  is the number of spatial locations,  $N_c$  is the number of coils, and  $N_t$  is the number of RF samples. Since  $N_s$  becomes unbearably large in designs such as 2D plus spectral and 3D problems, and  $N_c$  increases with more advance hardware designs, this  $\mathbf{A}$  matrix is typically too large to find the inverse in terms of memory. Therefore, such design problems need to be solved by iterative conjugate-gradient (CG) methods which avoid matrix inversion. However, even if no matrix inversions are performed, the large system matrix may still be memory-inefficient when used in many matrix multiplications over a large number of iterations, making the solving process very slow. Furthermore, the NUFFT-based pulse design methods can also be slow due to all the gridding steps. Although these can be eliminated in NUFFT-based image reconstruction using Toeplitz formulation, in RF pulse design the Toeplitz formulation does not exist since the inner product is over space. These slow design methods are especially undesirable when tailored pulses are needed to be designed for each subject during one's examination in the scanner. Typically, the subject-tailored pulse design has to be done within one minute in the pre-scan stage, so that the incorporation of subject-tailored pulses into currently used workflow is practical and desirable.

One application of subject-tailored multidimensional pTx pulses that is of particular interest of this dissertation is the 3D inner volume suppression (IVS) pulses for MR Corticography

(MRCoG). MRCoG is a developing imaging technique which aims for submillimeter isotropic resolution whole-cortex and cortex-specific imaging. It is a promising technique to enable whole-brain functional and diffusion studies of the columnar and laminar subcortical structures, which are the fundamentals of higher-order brain functions. MRCoG will use IVS to enable highly accelerated imaging of the cortex, by reducing g-factor and suppressing physiological noise from ventricle CSF. Therefore, subject-tailored IVS pTx pulses are needed, which could be applied before each excitation and readout. Thanks to the high performance gradient system and the 24-channel transmit system of the developing MRCoG scanner, good IVS with 3D selective excitation pulses becomes feasible. However, this IVS pulse design problem is challenging due to its 3D nature and the large number of transmit channels.

Here we propose a k-space-based approach to pTx pulse design that has low memory and computational requirements, and is highly parallelizable. Specifically, we build a sparse system matrix  $\mathbf{W}$  that relates the Fourier transform of the spatial domain desired pattern and the desired RF pulse, so that the RF pulse can be instantaneously solved by a sparse matrix multiplication with no matrix inversion or iterative CG method. We advance the work by Katscher et al [4] by solving the columns of the system matrix in a parallelized fashion. This is done by utilizing the independence between columns of the system matrix which comes from the compactness of sensitivity maps in k-space. In the following text, we will derive the independent solution to each column and show a patch-wise parallelization that allows the control of the size and accuracy of each instance problem. We further accelerate the solution of each instance problem by proposing an efficient method to construct a key matrix needed while maintaining accuracy. Off-resonance correction is also incorporated into this k-space domain design. Then we apply this k-space domain design method to the 3D IVS pulse design problem, and demonstrate its striking acceleration to the computation speed by comparing its performance to the conventional spatial domain design method through simulations. We show how the computation speed and accuracy can be traded off through controlling the parameters of the patch-wise parallelization. We also demonstrate the k-space domain design's ability to accommodate excitation k-space undersampling and correct off-

resonance.

## Theory

### k-space domain parallel-transmit pulse design

Here we describe the derivation of the highly parallelizable k-space domain design method. We propose to find a system matrix  $\mathbf{W}$  that directly maps a desired excitation pattern in k-space  $\mathcal{F}(\mathbf{d})$ , which is the Fourier transform of the spatial domain desired pattern  $\mathbf{d}$ , to the corresponding desired RF pulse  $\mathbf{b}$ , as:

$$\mathbf{b} = \mathbf{W}\mathcal{F}(\mathbf{d})$$

$\mathcal{F}(\mathbf{d})$  is the vectorized k-space excitation pattern with length of  $N_s$ , which is the number of spatial/k-space locations.  $\mathbf{b}$  is the concatenated multi-channel RF samples with length of  $N_t N_c$ , where  $N_t$  and  $N_c$  are the numbers of time points and coils, respectively.  $\mathbf{W}$  is the  $N_t N_c$  by  $N_s$  system matrix, which will latter be shown sparse. Therefore, once the  $\mathbf{W}$  matrix is found, the RF design problem can be instantaneously solved by a sparse matrix multiplication, and there is no matrix inversion or iterative CG method needed. Furthermore, in design problems involved iterative procedures, such as the phase updates in magnitude-least-squares pulse designs [7] and the regularization factor updates in power/roughness constrained pulse design, the sparsity of the  $\mathbf{W}$  matrix makes the iterative process much more efficient in terms of memory and speed. In the work of Katscher et al [4], parallel transmit pulse design was also formulated in the k-space domain. However, in Ref [4], the matrix  $\mathbf{W}$  was solved as a whole, which required constructing and inverting a large  $\mathbf{S}^H \mathbf{S}$  matrix, which will be explained in the following text. Our proposed method finely divides the process of finding  $\mathbf{W}$  into many independent instances, which allows the use of parallel computing to largely accelerate the computation. Furthermore, the  $\mathbf{S}^H \mathbf{S}$  matrices of different instances are each small, and our proposed method efficiently constructs these matrices, which further accelerates the computation.

We can solve for the columns of the  $\mathbf{W}$  matrix independently to each other, based on the

key observation that if the desired k-space pattern is a delta function at a given k-space location  $\vec{k}_i$  ( $1 \leq i \leq N_s$ ), then only the  $i$ -th column  $\mathbf{w}_i$  of  $\mathbf{W}$  relates the desired k-space pattern to the desired RF pulse. In this case, the vector  $\mathbf{w}_i$  is identical to the desired RF. Therefore, the question of finding the  $i$ -th column  $\mathbf{w}_i$  of  $\mathbf{W}$  can be restated as the following: what should the RF pulse samples be in order to generate a unit delta function at the location  $\vec{k}_i$  in k-space, and zeros elsewhere. Mathematically, the relationship that should be satisfied by the weights in column  $\mathbf{w}_i$  can be expressed as [4]:

$$\delta(\vec{k} - \vec{k}_i) = \sum_{t=1}^{N_t} \sum_{c=1}^{N_c} w_c(\vec{k}_t) \mathbf{s}_c(\vec{k} - \vec{k}_t) \quad [1]$$

where  $t$  indexes RF samples on the pulses excitation k-space trajectory, and  $c$  indexes coils.  $w_c(\vec{k}_t)$  is the  $((c-1)Nt + t)$ -th element of the  $\mathbf{w}_i$  vector.  $s_c(\vec{k} - \vec{k}_t)$  is the Fourier transform of coil- $c$ 's  $B_1^+$  map, shifted to be centered at excitation k-space location  $\vec{k}_t$ . This relationship can be restated in a matrix-vector form as:

$$\mathbf{S}\mathbf{w}_i = \delta_i \quad [2]$$

and the regularized pseudoinverse solution for the weight  $\mathbf{w}_i$  is

$$\mathbf{w}_i = (\mathbf{S}^H \mathbf{S} + \lambda \mathbf{I})^{-1} \mathbf{s}_i^H \quad [3]$$

where  $\mathbf{S}$  is the  $N_s$  by  $N_c N_t$  sensitivity matrix consisting of horizontally stacked  $\mathbf{s}_c(\vec{k} - \vec{k}_t)$  vectors for all  $c$  and  $t$ , and  $\mathbf{s}_i^H$  is the conjugate transpose of the  $i$ -th row of  $\mathbf{S}$ . Since k-space sensitivity maps are localized around DC, only few elements in  $\mathbf{s}_i^H$  and  $\mathbf{w}_i$  corresponding to  $\vec{k}_t$ s near  $\vec{k}_i$  are non-zero. In other words, only few RF samples on the excitation trajectory near the target  $\vec{k}_i$  can and should contribute energy to the unit delta function at this location, and all other RF samples on the excitation trajectory should automatically be zero. Therefore, in Equation 1, only few subscript  $t$ s are needed in the summation, and in Equation 2 and 3, the size of matrix  $\mathbf{S}$  is much smaller than it was defined in Ref [4]. It also indicates the system matrix  $\mathbf{W}$  is sparse. Techniques for efficient parallelization of the computation of the column  $\mathbf{w}_i$ s and efficient construction of the  $\mathbf{S}^H \mathbf{S}$  matrices are also developed and will be discussed in the following text.

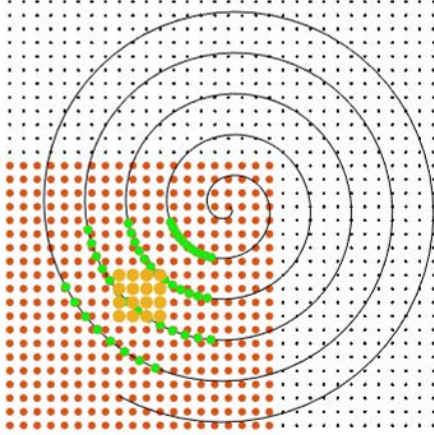


Figure 1: Illustration of one instance within the palatalization of a 2D k-space domain design problem. The totally design problem is divided into patches of width 4 cycle/FOV, and the 16 yellow points are the target points in this instance. With inclusion width of 4 cycle/FOV, the 46 green excitation trajectory points within the 12 cycle/FOV wide green square (4 cycle/FOV extended outside of the patch) are considered in this instance. The excitation within the 20 cycle/FOV wide red patch is constrained to zero except the point where the delta function is.

## Parallelization

A key advantage of the proposed pulse design formalism is that it can be broken down into many small problems and finely parallelized, because the process of solving each column of  $\mathbf{W}$  is independent of other columns. The columns can be solved fully independently, or patchwise for target locations in neighborhoods, wherein all points in the neighborhood share the same  $\mathbf{S}^H \mathbf{S}$  matrix. An example of this concept is shown in Figure 1. For simplicity of visualization, it is demonstrated in a 2D problem, but the concept is easily extended to 3D. The figure depicts the solution of the  $\mathbf{W}$  matrix 16 columns at a time, whose corresponding delta functions live within a patch of width 4 cycle/FOV (yellow points in Figure 1). In this instance where the inclusion width is also 4 cycle/FOV, we truncate the  $B_1^+$  map Fourier transforms to zero outside a 4 by 4 cycle/FOV square centered at DC. As a result, we must consider all the excitation trajectory points within a 12 by 12

cycle/FOV square, which is 4 cycle/FOV extended outside of the patch width 4 square, since they may contribute energy to the target locations corresponding to the 16  $\mathbf{W}$  matrix columns. For a single instance of the 16-point target patch shown in Figure 1, the 46 green points on the excitation trajectory may contribute significant energy and are considered in the weight design. Furthermore, we must constrain the total excitation to zero at all k-space locations within a 20 by 20 cycle/FOV red patch in Figure 1. This is because any energy deposited at each considered excitation trajectory points will affect not only the target points in the yellow square, but also the whole  $2 \times 4$  wide patch around that trajectory point. And the 20 by 20 cycle/FOV red patch is the total of the points that can be affected by all the excitation trajectory points considered in this instance. Therefore, in the solution for this instance,  $\mathbf{w}$  is a  $46N_c \times 16$  matrix,  $\mathbf{S}$  is a  $400N_c \times 46N_c$  matrix,  $\mathbf{S}^H\mathbf{S}$  is a  $46N_c \times 46N_c$  matrix, and  $\mathbf{s}_i^H$  is a  $46N_c \times 16$  matrix. In the next instance, another 16 columns centered around another 4 points by 4 points patch will be solved. It should be noted that in different instances, the number of neighboring excitation trajectory points (the 46 green points in the previous instance) can vary. We will denote this number of points by  $N_n$ .  $N_n$  can be zero when a patch is at the corners where no excitation trajectory point is adjacent.

The patch width determines the total number of instances to be solved. The inclusion width determines the accuracy of  $B_1^+$  information utilized in the design. Together, the patch width and the inclusion width determine how many excitation trajectory points are included in each instance, which further determines the size of  $\mathbf{S}^H\mathbf{S}$  whose construction is most computationally burdensome within an instance. Therefore, increasing patch width reduces the number of  $\mathbf{S}^H\mathbf{S}$  matrices to be constructed but increases the burden of constructing each of them. An optimal patch width should be decided case by case for different excitation trajectories.

### **Efficient construction of $\mathbf{S}^H\mathbf{S}$ matrix**

Constructing  $\mathbf{S}^H\mathbf{S}$  by finding  $\mathbf{S}$  is computationally expensive. As described previously, the  $((c - 1)N_c + t)$ -th column of the  $\mathbf{S}$  matrix,  $\mathbf{S}_c(\vec{k} - \vec{k}_t)$ , is the k-space sensitivity map of the  $c$ -th coil  $\mathbf{S}_c(\vec{k})$  shifted to excitation k-space trajectory location  $\vec{k}_t$ . These shifts for each column of  $\mathbf{S}$  are achieved

by applying a linear phase modulation to the spatial domain  $B_1^+$  map, followed by a fast Fourier transform (FFT). This process becomes computationally overwhelming when there are many RF samples, which is often the case. Furthermore, the matrix multiplication between  $\mathbf{S}^H$  and  $\mathbf{S}$  is also computationally intensive due to the large row dimension of  $\mathbf{S}$  ( $400N_t$  in the above example in Figure 1).

Inspired by a rapid GRAPPA calibration method for arbitrary 2D/3D non-Cartesian trajectories proposed in Ref [8], we have developed a fast and memory-efficient algorithm to solve this problem. A key innovation of Ref [8] is that the algorithm constructs the Hermitian  $\mathbf{S}^H\mathbf{S}$  matrix directly by finding each of the matrix's lower triangle elements through interpolation, instead of building the  $\mathbf{S}$  matrix explicitly followed by matrix multiplication. Conceptually, each element in the Hermitian matrix  $\mathbf{S}^H\mathbf{S}$  is the vector sum of two shifted k-space sensitivity maps, which is also one single point of their convolution. With the multiplication property of Fourier transform, this convolution in k-space can be calculated from the Fourier transform of the dot product of the two spatial domain  $B_1^+$  maps. For a more detailed derivation, please refer to Ref [8]. In practice,  $\mathbf{S}^H\mathbf{S}$  is constructed in the following way. We first represent the  $\mathbf{S}^H\mathbf{S}$  matrix with block matrices. Each block matrix  $\mathbf{S}_i^H\mathbf{S}_j$  is of size  $N_n$  by  $N_n$ , and  $\mathbf{S}_i$  and  $\mathbf{S}_j$  are the columns of  $\mathbf{S}$  related to the k-space sensitivity maps of the  $i$ -th and  $j$ -th coils respectively.

$$\mathbf{S}^H\mathbf{S} = \begin{pmatrix} \mathbf{S}_1^H\mathbf{S}_1 & \cdots & \mathbf{S}_1^H\mathbf{S}_{N_c} \\ \vdots & \ddots & \vdots \\ \mathbf{S}_{N_c}^H\mathbf{S}_1 & \cdots & \mathbf{S}_{N_c}^H\mathbf{S}_{N_c} \end{pmatrix} \quad [4]$$

Since  $\mathbf{S}^H\mathbf{S}$  is Hermitian, we only need to find the values within the lower triangle of the matrix, which are the lower triangle blocks  $\mathbf{S}_i^H\mathbf{S}_j$  with  $i > j$ . For a given lower triangle block  $\mathbf{S}_i^H\mathbf{S}_j$  ( $i > j$ ), all of its elements are interpolated from the densely sampled Fourier transform of the dot product of the spatial domain  $B_1^+$  maps of the  $i$ -th and  $j$ -th coils. The  $(m, n)$ -th element is the value interpolated at  $(\vec{k}_m - \vec{k}_n)$  away from DC. Therefore, to solve all the columns of  $\mathbf{W}$ , the total number of FFT operations needed in this efficient method is only  $N_c(N_c + 1)/2$ , instead of  $N_t N_c$ ,

and the storage size is also much smaller. In addition to the efficiency related to FFT, this algorithm saves a large matrix multiplication between  $\mathbf{S}^H$  and  $\mathbf{S}$  for the solving of every single column of  $\mathbf{W}$ . Although an alternative strategy of determining each column of  $\mathbf{S}$  explicitly by interpolating the  $N_s$  sample points from unshifted  $B_1^+$  Fourier transforms can also reduce the number of FFT operations, it still has the problem of large multiplications between  $\mathbf{S}^H$  and  $\mathbf{S}$  matrices. Furthermore, to calculate each element of  $\mathbf{S}^H \mathbf{S}$ , there are  $2N_s$  number of interpolations involved with this sub-optimal strategy. While with the efficient algorithm there is only one interpolation from the densely sampled Fourier Transform of the dot product of two spatial domain  $B_1^+$  maps needed. The extra interpolations involved in the sub-optimal strategy would introduce a larger error to  $\mathbf{S}^H \mathbf{S}$ .

### Off-Resonance correction

As shown in Equation ?? when we introduced spatial domain design in Chapter ??, the equation connecting a pTx pulse to its excitation pattern has an off-resonance dependent term  $e^{i\gamma\Delta B_0(\mathbf{x})(t-T)}$ . In order to model this off-resonance dependent term in our k-space domain design, we adapted a fast implementation of the off-resonance compensation with time segmentation approximation and weighted least-squares interpolators [9]. By segmenting the RF pulse into multiple segments, this method disentangles the space-and-time dependent phase accrual induced by main field inhomogeneity into either space- or time- dependent terms, and therefore a same system matrix can be applied within each segment. Mathematically, it is

$$e^{i\Delta\omega_j(t_i-T)} = \sum_{l=1}^L b_l(t_i) e^{i\theta_l(\Delta\omega_j)}$$

where  $i = 1 \dots N_t$  indexes the RF samples,  $j = 1 \dots N_s$  indexes the spatial locations, and  $l$  indexes the time segments. The left term is the problematic space-and-time dependent term, with  $\Delta\omega_j$  representing the off-resonance at the location- $j$  obtained from a field map and  $T$  being the pulse duration.  $b_{il} = b_l(t_i)$  are the time-dependent-only weights called temporal interpolators applied upon RF samples.  $c_{lj} = e^{i\theta_l(\Delta\omega_j)}$  are the space-dependent-only phase accrual called spatial interpolators, applied upon the excitation pattern of each weighted RF segment. Therefore, the off-

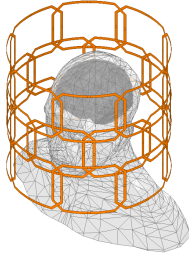


Figure 2: 24-channel loop Tx array. The array has diameter 32 cm and height 28 cm. The 16 cm *times* 11 cm loops are arranged in 3 rows of 8.

resonance correcting RF can be obtained by

$$\mathbf{b} = \sum_{l=1}^L \text{diag}\{\mathbf{b}_l\} \mathbf{W} \mathcal{F}(\text{diag}\{\mathbf{c}_l\} \mathbf{d})$$

where  $\mathbf{b}_l$  and  $\mathbf{c}_l$  are the vectorized interpolators for the  $l$ -th segment.

## Methods

RF pulses were designed for the 24-channel loop transmit array (Figure 2) that will be built for the MRCoG scanner and compressed to 16 channels using array compressed parallel transmission [10].  $B_1^+$  maps used in the pulse design were simulated in a human head model using Ansys High Frequency Structure Simulator (Canonsburg, PA, USA) with 1.5 mm isotropic resolution. A SPINS trajectory [11] (Figure 3a&b) with 5 mm max resolution was empirically designed for the pulse. The gradient duration was minimized to 10 ms through time-optimal design [12] subject to the proposed MRCoG scanners gradient amplitude and slew rate constraints of 200 mT/m and 700T/m/s, respectively.

Figure 3a shows the target pattern for the pulse design shaped as an ellipse centered on the ventricles with AP/HF/LR semi-axes of 4.8/3.2/3.2 cm. The target pattern was smoothed by a Fermi filter. Pulses were designed to excite the entire ellipse and achieve zero excitation in voxels in the cerebrum but outside the ellipse. Both the smoothed target pattern and the  $B_1^+$  maps

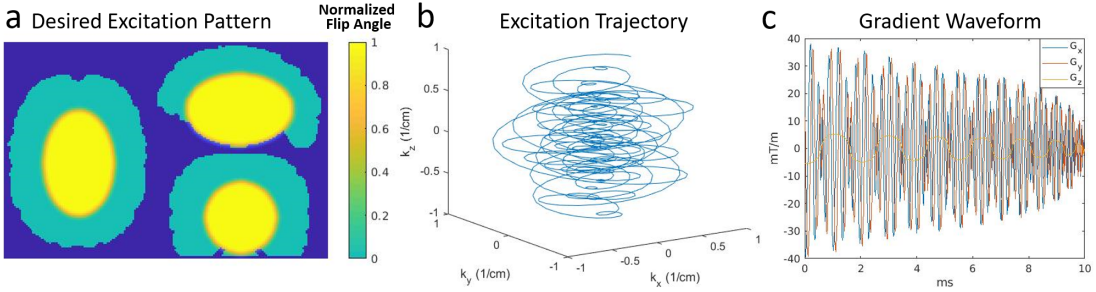


Figure 3: (a) Target excitation pattern for the IVS pulses. (b) 10 ms SPIN trajectory used in the designs. (c) Gradient waveforms of the excitation trajectory.

were undersampled from  $128 \times 128 \times 96$  grids (1.5mm iso-resolution) into  $64 \times 64 \times 48$  grids (3mm iso-resolution). The RF designs were done with the  $64 \times 64 \times 48$  grid size. The resulted pulses were evaluated against the target pattern with the  $128 \times 128 \times 96$  grid in order to expose Gibbs ringing. The normalized root-mean-square error (NRMS) was calculated against the voxels within the cerebrum.

With conventional spatial domain design, RF pulses were solved using an iterative least-squares conjugate-gradient decent method [6]. With the proposed k-space domain design, RF pulses were solved with different parallelization parameters: thread number, patch width, and inclusion width. In order to study the computational acceleration provided by parallel computing, the design problem was solved with thread numbers ranging from 1 to 32, while the patch width and inclusion width were both set to 4. In order to study the computation time and error with respect to different patch widths and inclusion widths, we then held the computing threads constant at 16 while varying the patch and inclusion widths. The computation was done on a computer with a 512 GB RAM and two 24-core 2.1 GHz Intel Xeon CPUs which provides maximum 94 threads. For each design case, the computation was run 5 times, and the mean computation time and the NRMSE were recorded.

In order to demonstrate the k-space domain designs robustness to Gibbs ringing, the target pattern and  $B1^+$  maps were down-sampled into  $32 \times 32 \times 24$  (6mm iso-resolution) and  $64 \times 64 \times 48$  grids (3mm iso-resolution). The outer sections of the excitation trajectory, equaling 2.1 ms, was

excluded so that the maximum excitation resolution matched with the chosen 6 mm iso-resolution. All three designs were evaluated against the target pattern with the fully sampled  $128 \times 128 \times 96$  grid for validation.

The k-space domain design method's performance regarding k-space undersampling, which is desired for shorter pulse duration, was also examined and compared against the spatial domain design. The undersampling was achieved by reducing the numbers of the previously specified SPIN trajectory's polar and azimuthal rotations proportionally by a factor called acceleration factor, as shown in the third row of Figure 7.

In order to show the k-space domain design method's ability to compensate moderate off-resonance and compare it against the spatial domain method. We incorporated a normalized field map with Gaussian inhomogeneity centered above the frontal sinus (Figure 8a), mimicking a characteristic susceptibility induced  $B_0$  inhomogeneity. The field maps were then scaled so that the maximum off-resonance reached +100 Hz, +200 Hz, and +300 Hz. Off-resonance corrected spatial domain designs were done with system matrices whose field maps were also incorporated through time segmentation approximation [9]. k-space domain design were done with or without off-resonance correction.

## Results

Figure 4a shows the mean computation time versus different thread numbers. The k-space design problem held the patch and inclusion width constant at 4. The mean computation time decreases with increasing thread numbers before 12 threads, and then plateaus due to overhead. The thread number was conservatively chosen to be 16 for the following studies to ensure timely solutions. Figure 4b shows the mean computation time and the NRMSE with different patch widths. The computation time increases and the NRMSE decreases as the patch width increases. This was because when patch width increases, there are more excitation trajectory points included in one instance problem, even with the same inclusion width. As a result, each instance problem becomes bigger and more time consuming, which cancels the advantageous fact that there are fewer instance

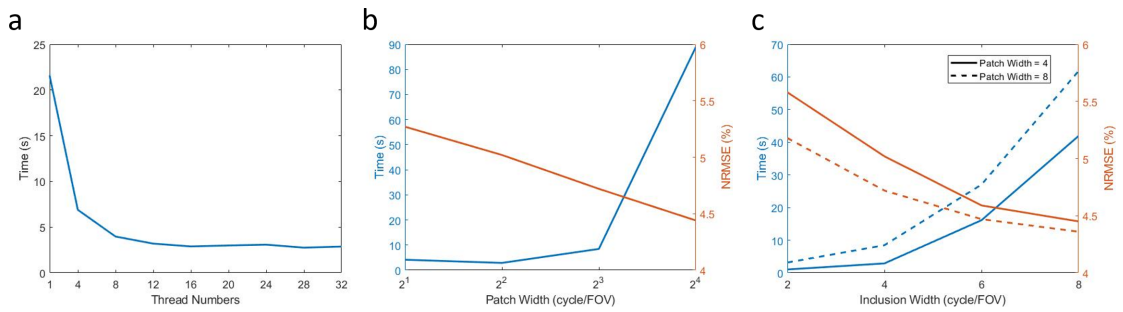


Figure 4: Studies of different parallelization parameters, where patch width is the square root of the number of  $\mathbf{W}$  columns solved for simultaneously and inclusion width is the assumed range of influence of each excitation k-space location. **(a)** Computation time vs. thread numbers. Patch width and inclusion width were kept at 4 cycle/FOV. **(b&c)** Computation time (blue axis) and NRMSE (red axis) vs. patch widths (b) and inclusion widths (c). Thread number were kept at 16 for both designs. Inclusion width was constant at 4 in (b) and patch widths were constant at 4 (solid line) and 8 (dashed line).

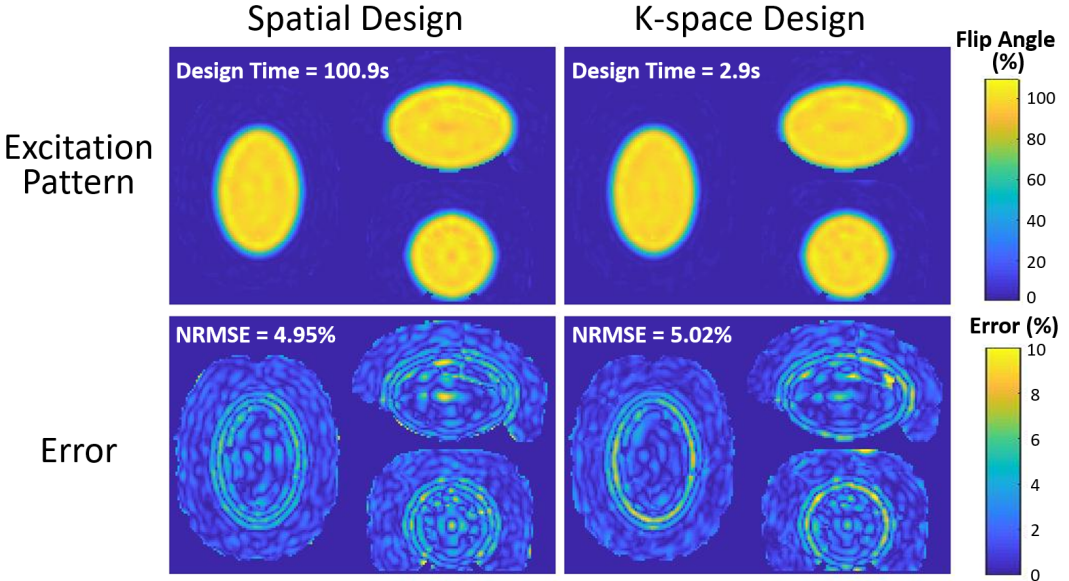


Figure 5: Normalized excitation patterns (top row) and error maps (bottom row) for k-space domain design (left column) and spatial domain design (right column), with NRMSE and design time indicated.

problems in total, especially in cases with parallel computing. Furthermore, increasing the patch width is equivalently increasing the inclusion widths for the center target points within each patch, which makes the solutions more accurate. Here, we chose patch widths 4 and 8 (labeled  $2^2$  and  $2^3$ ) to balance time and accuracy for further evaluation. Figure 4c shows the mean computation time and the NRMSE with different inclusion widths. The solid lines and dashed lines were obtained with patch width 4 and 8, respectively. Computation time increases and error decreases with increasing inclusion width. Particularly, increasing inclusion width is equivalent to utilizing more accurate  $B_1^+$  information by truncating the  $B_1^+$  map Fourier transforms to zero further out from DC. For both patch widths 4 and 8, 4 is the optimal inclusion width, which confirms the result in 4a , previously. Using an inclusion width of 4, the computation time and error are acceptable for both patch width numbers. Following these results, we chose patch width 4 for the further designs.

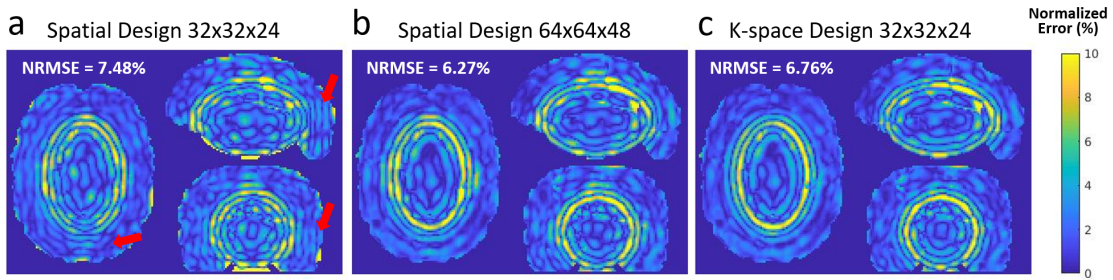


Figure 6: Normalized error maps and NRMSE for (a) spatial domain design and (c) k-space domain design with 6 mm iso-resolution,  $32 \times 32 \times 24$  design grid. Red arrows indicate the Gibbs ringing in low-resolution spatial domain design. (b) Normalized error map for spatial domain design with 3 mm iso-resolution,  $64 \times 64 \times 48$  design grid.

The normalized excitation patterns and error maps are shown in Fig 5 for both k-space domain design (left) and spatial domain design (right), where the k-space domain design was solved with 16 parallel computing threads, patch width 4, and inclusion width 4. Both designs were done with the  $64 \times 64 \times 48$  grid size (3mm iso-resolution), and the excitation patterns were evaluated against the target pattern with the  $128 \times 128 \times 96$  grid size (1.5mm iso-resolution). The calculated NRMSE from the k-space domain design and the spatial domain design were 5.02% and 4.94%, respectively, which were practically equal. For both design methods, most of the errors appeared at the edges of the transition band, with other errors lower than 5% of the target flip angle. This indicates uniform inner volume suppression while maintaining the outer volume intact, which can in turn decrease g-factor in highly accelerated imaging. In practice, error near the transition band can be mitigated by ensuring the region of interest (ROI) of the cortex falls completely in the stop-band and assuming zero signal within the pass-band during undersampled reconstruction. More significantly, the parallelized k-space domain design method drastically reduced the mean computation time from 100.9 seconds to 2.9 seconds compared to the spatial domain design, which was a 97% decrease.

Figure 6a&c show the results of the low-resolution designs using k-space domain method and the spatial domain method. The result of the high-resolution design of the spatial domain is also shown in Figure 6b. All three designed were done with a excitation trajectory that matches the 6 mm iso-resolution. The red arrows indicate the Gibbs ringing in the low-resolution spatial domain design, that can only be suppressed with high-resolution spatial domain design. However, the k-space domain design, although also low-resolution, is insensitive to this problem. Furthermore, the ripple pattern in the low resolution k-space design matches the high-resolution spatial design. Looking from a spatial domain point of view, the Gibbs ringing was caused by the lack of ability to observe the ringing with low-resolution. Looking from a k-space domain point of view, the Gibbs ringing was due to "wrap back" of the k-space FOV. When the spatial resolution is low the k-space FOV is small, and therefore the RF samples at one end of the trajectory can incorrectly "reach" and affect the k-space points at the other end of the k-space FOV in a circulation shift fashion. However, for the k-space domain design, even with low resolution, there is no k-space "wrap back" because the incorporated trajectory points are explicitly specified. Particularly, for the instance problems whose patches are at the edges of the k-space FOV, the excitation trajectory points at the other ends of the k-space FOV will not be incorporated into the design.

Figure 7 shows a comparison between the performance of spatial domain design (first row) and k-space domain design (second row) regarding undersampled excitation trajectories (third row) with different acceleration factors. Both design methods had larger errors when the excitation k-space was less densely traversed. The k-space domain design provided similar error maps and practically equal NRMSE. The k-space domain design had slightly larger NRMSE because of the interpolation and truncation of the k-space sensitivity when building the  $\mathbf{S}^H \mathbf{S}$  matrix, and can be improved by increasing the inclusion width.

Regarding 3D off-resonance patterns with the shape shown in Figure 8a and different scaling, Figure 8b shows the excitation maps of three types of designs: spatial domain design with off-resonance correction (first row), k-space domain design with and without off-resonance correction (second & third row). As shown in the second row of Figure 8b, off-resonance caused false excita-

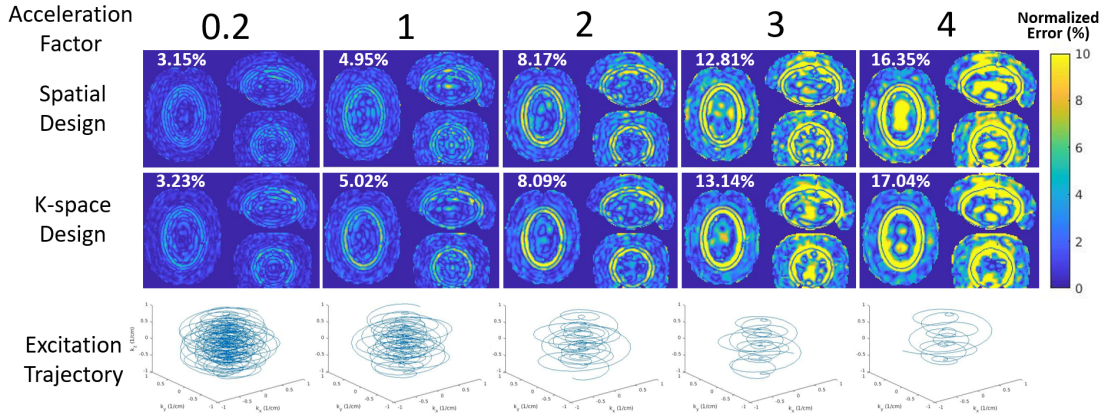


Figure 7: Normalized error maps and RMSE for spatial domain design (first row) and k-space domain design (second row), with excitation trajectories undersampled by different acceleration factors (third row).

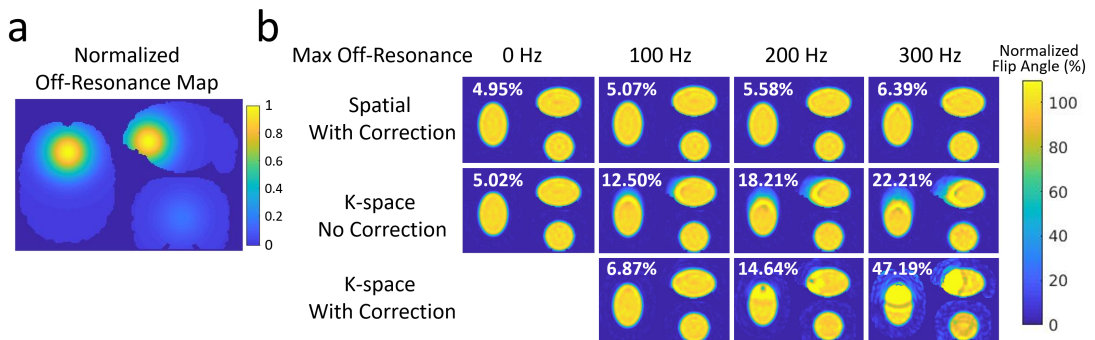


Figure 8: (a) Normalized off-resonance map with Gaussian distortion centered above the frontal sinus, mimicking a characteristic susceptibility induced  $B_0$  inhomogeneity. (b) Normalized excitation maps and RMSE for spatial domain design with off-resonance correction (first row), k-space domain design with and without off-resonance correction (second & third rows).

tion outside the designated suppression region, and must be corrected. k-space domain design with correction was able to correct off-resonance artifacts and provide excitation patterns comparable to spatial domain design, for maximum off-resonance up to 200 Hz, which is the typical range of off-resonance observed in clinical studies. The k-space domain design has a weaker performance with higher off-resonance due to the fact that the time segmentation approximation in Ref [9] was meant to approximate forward models from RF to excitation patterns and does not serve as an accurate approximation to the backward model as we need in the k-space domain design.

## Discussion and Conclusions

A computationally efficient and highly parallelizable k-space domain pTx pulse design method was proposed. The method adapts the k-space domain formulism proposed by Katscher et al [4], which does not require the computationally expensive iterative processes in the conventional spatial domain design methods. The method advances the work of Katscher et al [4] by finely parallelizing the process of finding the system matrix. Furthermore, a technique inspired by a rapid GRAPPA calibration method [8] is also included to further speed up the computation of each instance. The proposed k-space domain design method was evaluated through simulation upon an inner volume pulse design problem for MR Corticography, which can in turn enable submillimeter whole-cortex and cortex-specific imaging. The optimal parallelization parameters: thread number, patch width, and inclusion width, were found for this design problem. The proposed method reduced the computation time by 97% compared to the conventional spatial domain design method, while producing equal inner volume suppression performance. And the abilities of the proposed method to accommodate k-space undersampling and correct off-resonance were also demonstrated to be equal to conventional spatial domain design method.

## References

- [1] Susanne Rieseberg, Jens Frahm, and Jürgen Finsterbusch. Two-dimensional spatially-selective rf excitation pulses in echo-planar imaging. *Magnetic Resonance in Medicine: An Official Journal of the International Society for Magnetic Resonance in Medicine*, 47(6):1186–1193, 2002.
- [2] Suwit Saekho, Fernando E Boada, Douglas C Noll, and V Andrew Stenger. Small tip angle three-dimensional tailored radiofrequency slab-select pulse for reduced b1 inhomogeneity at 3 t. *Magnetic Resonance in Medicine: An Official Journal of the International Society for Magnetic Resonance in Medicine*, 53(2):479–484, 2005.
- [3] V Andrew Stenger, Fernando E Boada, and Douglas C Noll. Three-dimensional tailored RF pulses for the reduction of susceptibility artifacts in  $T_2^*$ -weighted functional MRI. *Magn Reson Med*, 44(4):525–531, 2000.
- [4] Ulrich Katscher, Peter Börnert, Christoph Leussler, and Johan S Van Den Brink. Transmit sense. *Magnetic Resonance in Medicine: An Official Journal of the International Society for Magnetic Resonance in Medicine*, 49(1):144–150, 2003.
- [5] Y Zhu. Parallel excitation with an array of transmit coils. *Magn Reson Med*, 51(4):775–784, 2004.
- [6] W A Grissom, C Y Yip, Z Zhang, V A Stenger, J A Fessler, and D C Noll. Spatial domain method for the design of RF pulses in multicoil parallel excitation. *Magn Reson Med*, 56(3):620–9, Sep 2006.
- [7] K Setsompop, LL Wald, V Alagappan, BA Gagoski, and E Adalsteinsson. Magnitude least squares optimization for parallel radio frequency excitation design demonstrated at 7 Tesla with eight channels. *Magn Reson Med*, 59(4):908–915, 2008.

- [8] Tianrui Luo, Douglas C Noll, Jeffrey A Fessler, and Jon-Fredrik Nielsen. A grappa algorithm for arbitrary 2d/3d non-cartesian sampling trajectories with rapid calibration. *Magnetic resonance in medicine*, 82(3):1101–1112, 2019.
- [9] Jeffrey A Fessler, Sangwoo Lee, Valur T Olafsson, Hugo R Shi, and Douglas C Noll. Toeplitz-based iterative image reconstruction for mri with correction for magnetic field inhomogeneity. *IEEE Transactions on Signal Processing*, 53(9):3393–3402, 2005.
- [10] Zhipeng Cao, Xinqiang Yan, and William A Grissom. Array-compressed parallel transmit pulse design. *Magnetic resonance in medicine*, 76(4):1158–1169, 2016.
- [11] Shaihan J Malik, Shiva Keihaninejad, Alexander Hammers, and Joseph V Hajnal. Tailored excitation in 3d with spiral nonselective (spins) rf pulses. *Magnetic resonance in medicine*, 67(5):1303–1315, 2012.
- [12] Michael Lustig, Seung-Jean Kim, and John M Pauly. A fast method for designing time-optimal gradient waveforms for arbitrary k-space trajectories. *IEEE transactions on medical imaging*, 27(6):866–873, 2008.